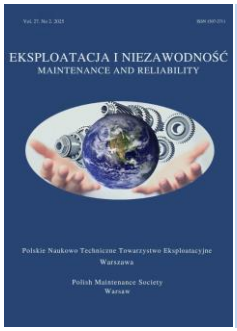


# Eksploatacja i Niezawodnosc – Maintenance and Reliability

**Volume 27 (2025), Issue 2**

journal homepage: http://www.ein.org.pl

Article citation info:
Gao H, Wang Y, Xu J, Qin H, Fatigue strength reliability assessment of turbofan blades subjected to intake disturbances based on the improved kriging model, Eksploatacja i Niezawodnosc – Maintenance and Reliability 2025: 27(2) http://doi.org/10.17531/ein/194175


# Fatigue strength reliability assessment of turbofan blades subjected to intake disturbances based on the improved Kriging model


Indexed by: Web of Science Group



**Hai-Feng Gao[a,*], Yuhang Wang[a], Jingjing Xu[a], Huibin Qin[b]**

[a] School of Mechatronic Engineering and Automation, Shanghai University, China.
[b] School of Mechanical Engineering, North University of China, China.


## Highlights

- The influence of intake disturbance on the vibration of turbofan blades was discussed.
- Dynamic analysis of structures subjected to multiple sinusoidal loads simultaneously.
- Calculate the reliability of fatigue strength for different vibration modes of blades.
- DCGAK improves the numerical and reliability prediction accuracy of complex systems.


## Abstract

This paper aims to develop an efficient and precise reliability analysis method to enhance the numerical prediction accuracy for complex structures. Kriging, an implicit surrogate model, used to address highly nonlinear and complex problems. In this study, genetic algorithms (GA) are utilized to optimize the parameters of the Kriging model, which is then integrated with a distributed collaborative strategy to introduce the Genetic Algorithm Optimized Distributed Collaborative Kriging Model (DCGAK). Using the CFM56-fan blade as a case study, the impact of intake disturbances at the engine inlet is evaluated to assess the fatigue strength reliability of the blade. Comparison with different mathematical models demonstrates that the prediction accuracy of DCGAK closely aligns with the Monte Carlo sampling results, suggesting promising prospects for its application in numerical prediction and reliability analysis. This approach enriches the current methods for structural reliability analysis of complex mechanical systems.



**Keywords**
Turbofan, fatigue strength reliability, genetic algorithm, kriging, distributed collaborative strategy




## 1. Introduction

High-bypass-ratio turbofan engines significantly enhance the thrust of aircraft engines while offering advantages such as low fuel consumption and reduced noise, making them the current trend in the aviation industry. However, large-sized blades face severe reliability challenges due to intensified vibrations caused by high aerodynamic and centrifugal loads.

Vibration is a major cause of structural fatigue failure, with resonance being particularly detrimental to structures. During the early design phase, engineers often use Campbell diagrams and frequency interference theory to avoid potential resonance points in turbofan blades during operation. Gao et al. used leave-one-out cross-validation least-squares support vector machine and SVM response surface methods to predict compressor blade natural frequencies for frequency margin design [1-2]. However, for structures with complex vibrations and multiple resonance modes, completely avoiding resonance points is often infeasible. In practice, it is essential to allow structures to operate under certain resonance conditions while


(*) Corresponding author.
E-mail addresses: H. Gao (ORCID: 0000-0001-6054-6417) gaohaifeng@shu.edu.cn, Y. Wang ,J. Xu, xjj125@shu.edu.cn, H. Qin

considering the stress state during resonance and avoiding dangerous resonance points that could lead to structural failure. Li et al. predicted the fatigue failure behavior and fatigue strength of Ni-based superalloy turbine blades under high-temperature conditions at 750°C [24]. Using a typical titanium-based high-temperature alloy compressor blade disk as an example, Wang et al. proposed a fuzzy least squares support vector regression method based on the randomization of fuzzy variables. They also provided a corresponding sampling-based probabilistic fatigue estimation framework [25]. Zhu et al. conducted experiments and finite element analysis on full-scale blade disks and performed importance ranking of random variables for the fatigue design of the blade disk. They established a computational-experimental framework for evaluating the fatigue reliability of turbine blades [26]. Given the high cost and time consumption associated with traditional experimental methods for determining fatigue strength, which can extend analysis and design cycles, Guo et al. proposed a method using Bayesian optimization to enhance the fatigue strength prediction of a Random Forest Regression (RFR) model. This approach helps mitigate issues of overfitting or underfitting [27]. Gao et al. simulated the vibration stress caused by simultaneous resonance of the first three modes and conducted fatigue strength reliability assessments [3].

For fan blades, forced vibration is primarily influenced by periodic aerodynamic loads. However, in actual operation, aircraft engines often encounter conditions such as large angles of attack and crosswinds, leading to unstable air distortion at the engine inlet, known as inlet distortion [7-9]. Inlet distortion frequently causes resonance in fan blades, resulting in performance degradation or even severe consequences such as significant bending or fractures [10]. However, most current studies only apply uniformly distributed aerodynamic loads on the surface of fan blades or set uniform inlet boundary conditions at the engine inlet. For example, Ma et al. estimated the probabilistic high-cycle fatigue life of blades under airflow excitation while considering fluid-structure interaction analysis, but they assumed uniform total temperature and pressure at the flow field inlet [28]. Liu et al., in their study of the response and high-cycle fatigue of a radial turbine under airflow excitation, only set uniform total pressure and temperature at the flow field inlet [29]. Gao, in the study of fatigue strength reliability analysis, only considered applying uniform fluid mass per second at the fan blade inlet [3]. In reality, the boundary conditions at the fan blade inlet and the aerodynamic loads on the surface are complex, making the scenarios considered in these studies overly idealized. Phan et al. considered differences in aerodynamic loads at different positions on the blade surface but studied the issue from the perspective of blade stagger angle rather than the flow field [30]. Lin, in assessing the fatigue life and reliability of fan blades, considered inlet distortion factors and different flow field inlet boundary conditions corresponding to different blade heights but focused on the radial aspect of the blade [31]. Zhang et al. studied the strength analysis of compressor blades under inlet distortion, confirming that circumferential total pressure distortion causes uneven aerodynamic forces distribution along the circumferential direction, significantly impacting fatigue strength. However, this study did not considered the dispersion of random variables and did not conduct a reliability analysis of fatigue strength [32]. In summary, this paper focuses on the fan blades of a high-bypass ratio turbofan engine, applying circumferential total pressure inlet distortion to the airflow field at the fan blade inlet, and evaluates the fatigue strength reliability of the fan blades under non-uniformly distributed aerodynamic loads.

Probabilistic reliability design of complex structures is a critical technology in need of breakthroughs. The probabilistic design methods offer a more realistic representation of structural response uncertainties compared to traditional safety factors or deterministic approaches, making efficient and accurate prediction models crucial for reliability probabilistic design. Existing probabilistic reliability methods include first-order second-moment methods, second-order second-moment methods, and second-order fourth-moment methods, but these methods often lack prediction accuracy for high-dimensional complex problems and cannot address implicit function issues. To overcome these limitations, many scholars have used response surface methods in place of limit state functions for reliability analysis [8-11]. Monte Carlo simulation (MCS), when the function or surrogate model of the structure and the probability distribution of random variables are known, performs statistical analysis on simulation results through numerous repetitive simulations. However, its complexity and lower computational efficiency make it more suitable for

validating the prediction accuracy of different algorithms [12].

The Kriging surrogate model is an unbiased estimation model with minimal variance, commonly used for high-dimensional, complex nonlinear problems [13]. To improve the fitting accuracy of the Kriging model, this paper optimizes the parameters through the genetic algorithms (GA) and integrates it with a distributed collaborative strategy, proposing the Genetic Algorithm Optimized Distributed Collaborative Kriging Model (DCGAK). This model is applied to assess the fatigue strength reliability of turbofan blades considering the impact of intake disturbances. Section 2 of this paper details the basic principles and mathematical models of DCGAK for reliability analysis, and verifies the method through numerical cases. Section 3 conducts a deterministic analysis of the turbofan blades, determining their natural frequency, surface aerodynamic loads, and actual high-cycle vibration stress at 83% design speed. Section 4 performs probabilistic analysis of the vibration stress, validates the effectiveness of the proposed model, and calculates fatigue strength reliability while comparing the accuracy of different models. Section 5 provides a summary and conclusion of the study.

## 2. Distributed collaborative GAK modeling

### 2.1. Kriging

The Kriging surrogate model is a regression algorithm based on covariance functions used for spatial modeling and prediction of stochastic processes [14]. Moreover, kernel function values in different directions of the input vectors can vary, allowing the Kriging surrogate model to achieve ideal results for both isotropic and anisotropic problems, and it has been widely applied in structural reliability assessment in recent years.

Currently, when using Kriging surrogate models to address regression problems, the implicit function relationship of the problem is often reconstructed in the following Gaussian form:

$$y(\boldsymbol{x}) = f^T(\boldsymbol{x})\boldsymbol{\beta} + z(\boldsymbol{x}) \tag{1}$$

where $f(\boldsymbol{x}) = \left[f_1(\boldsymbol{x}), f_2(\boldsymbol{x}), \dots, f_p(\boldsymbol{x})\right]^T$ represents the regression basis functions, and the parameter $p$ depends on the type of regression basis functions.

When $p = 1$, $f(x)$ represents a constant term regression basis function; when $p = n + 1$, $f(x)$ represents a first-order polynomial regression basis function; when $p = \frac{n^2+3n+2}{2}$, $f(x)$ represents a second-order polynomial regression basis function, as shown in Equation (2).

$$f(\boldsymbol{x}) = \begin{cases} 1, & \text{when } p = 1 \\ [1, x_1, x_2, \dots, x_n]^T, & \text{when } p = n + 1 \\ \left[1, x_1, \dots, x_p, x_1^2, \dots, x_1x_p, x_2^2, \dots, x_2x_p, x_p^2\right]^T, & \text{when } p = \dfrac{n^2+3n+2}{2} \end{cases} \tag{2}$$

In this paper, a constant term regression basis function is used to establish the DCGAK prediction model, and its accuracy meets the usage requirements.

In equation (1), $\boldsymbol{\beta} = \left[\beta_1, \beta_2, \dots, \beta_p\right]^T$ represents regression coefficients, and $z(x)$ is a Gaussian random process with the following statistical properties:

$$\begin{cases} E[z(x)] = 0 \\ Var[z(x)] = \sigma^2 \\ Cov\left[z(x_i), z(x_j)\right] = \sigma^2 R(x_i, x_j) \end{cases} \tag{3}$$

where $x_i$ and $x_j$ are any two input vectors; $\sigma^2$ is the process variance; $R(x_i, x_j)$ is the correlation model, defined as the product of the correlation functions in each dimension, and is expressed as follows:

$$R(x_i, x_j) = \prod_{k=1}^{n} \exp\left(-\theta_k \left|x_i^{(k)} - x_j^{(k)}\right|\right) = \exp\left(-\sum_{k=1}^{n} \theta_k \left|x_i^{(k)} - x_j^{(k)}\right|\right) \tag{4}$$

where $x_i^{(k)}$ is the k-th dimensional input variable of the input vector $x_i$; n is the dimension of the input vector. The correlation parameter $\theta_k$ describes the sensitivity of output variable to changes in the k-th dimensional input variable, representing the relative importance of $x^{(k)}$. The larger the $\theta_k$, the more the change in $x^{(k)}$ affects the value of $y(x)$. The input-output characteristics of the Kriging model are directly determined by the correlation parameters.

Assuming the sample points $\boldsymbol{x} = \{\boldsymbol{x_1}, \boldsymbol{x_2}, \dots, \boldsymbol{x_m}\}$ are known, with each sample corresponding to an output response $\boldsymbol{y} = [y(x_1), y(x_2), \dots, y(x_m)]^T$, and the initial correlation parameters $\boldsymbol{\theta} = \{\theta_1, \theta_2, \dots, \theta_m\}$, the estimates of the regression

coefficients $\boldsymbol{\beta}$ and process variance $\boldsymbol{\sigma}^2$ are as follows:

$$\begin{cases} \widehat{\boldsymbol{\beta}} = (\boldsymbol{F}^T\boldsymbol{R}^{-1}\boldsymbol{F})^{-1}\boldsymbol{F}^T\boldsymbol{R}^{-1}\boldsymbol{Y} \\ \widehat{\boldsymbol{\sigma}}^2 = \dfrac{1}{m}\left(\left(\boldsymbol{Y}-\boldsymbol{F}\widehat{\boldsymbol{\beta}}\right)^T\boldsymbol{R}^{-1}\left(\boldsymbol{Y}-\boldsymbol{F}\widehat{\boldsymbol{\beta}}\right)\right) \end{cases} \tag{5}$$

where $\boldsymbol{F}\in\mathbb{R}^{m\times p}$ is the regression basis function matrix, and the element in the $i$-th row and $j$-th column is $f_j(x_i)$; $\boldsymbol{R}\in\mathbb{R}^{m\times m}$ is the correlation function matrix, where the element in the $i$-th row and $j$-th column is $R(x_i, x_j)$.

Based on maximum likelihood estimation, the optimal correlation parameters $\boldsymbol{\theta}^*$ of the Gaussian random process can be solved using the following equation:

$$\boldsymbol{\theta}^* = \min_{\theta}\left\{\varphi(\boldsymbol{\theta}) \equiv |\boldsymbol{R}|^{\frac{1}{m}}\,\widehat{\boldsymbol{\sigma}}^2\right\} \tag{6}$$

After solving for the optimal correlation parameters $\boldsymbol{\theta}^*$, the best Kriging surrogate model form between the sample*s* and the output response $y$ is as follows:

$$\hat{y}(\boldsymbol{x}) = f^T(\boldsymbol{x})\widehat{\boldsymbol{\beta}} + r^T(\boldsymbol{x})\boldsymbol{R}^{-1}\left(\boldsymbol{Y}-\boldsymbol{F}\widehat{\boldsymbol{\beta}}\right) \tag{7}$$

The optimal correlation parameters $\boldsymbol{\theta}^*$ directly influence prediction performance of the Kriging model. Therefore, it is crucial to search for the optimal correlation parameters $\boldsymbol{\theta}^*$. In this paper, genetic algorithms will be used to find the optimal correlation parameters $\boldsymbol{\theta}^*$ for fitting the Kriging model.

### 2.2. GA-based Kriging model

GAK sets the correlation parameters $\boldsymbol{\theta}$ in the Kriging model as individuals in the genetic algorithm population. For problems with multiple input variables, the dimension of the correlation parameters $\boldsymbol{\theta}$ is consistent with the number of input variables. The function $\varphi(\boldsymbol{\theta})$ is used as the fitness function in the genetic algorithm to iteratively optimize the population individuals. Based on maximum likelihood estimation, the optimal correlation parameters $\boldsymbol{\theta}^*$ are obtained when the value of $\varphi(\boldsymbol{\theta})$ is minimized, which is then used to establish the optimal Kriging model.

Given the sample points $\boldsymbol{x} = \{\boldsymbol{x_1}, \boldsymbol{x_2}, \dots, \boldsymbol{x_m}\}$, with each sample corresponding to an output response $\boldsymbol{y} = [y(x_1), y(x_2), \dots, y(x_m)]^T$, the basic steps of the GAK model are as follows:

(1) Initialization: Set the correlation parameters $\boldsymbol{\theta} = \{\theta_1, \theta_2, \dots, \theta_m\}$ as individuals in the genetic algorithm population, with the number of correlation parameters matching the number of input variables. Define the range of individual values $[\boldsymbol{V_1}, \boldsymbol{V_2}]$, the maximum number of iterations $p_{max}$, the population size $k$, the number of genes $n$, and the population convergence criteria. Randomly generate a binary initial population and encode the chromosomes. In this paper, binary encoding is used, and the encoding format is as follows:

$$\boldsymbol{\theta}^{(k)} = \boldsymbol{V}_1 + \frac{\boldsymbol{V}_2 - \boldsymbol{V}_1}{2^n - 1} \times \left(\sum_{i=1}^{n} b_i \times 2^{i-1}\right) \tag{8}$$

where $\boldsymbol{\theta}^{(k)}$ represents the correlation parameters with upper and lower bounds $[\boldsymbol{V_1}, \boldsymbol{V_2}]$, encoded as a binary string of length $n$ (denoted as $b_n \dots b_2 b_1$). After encoding, the population matrix is represented as follows:

$$\left[b_n^{(1)} \dots b_2^{(1)} b_1^{(1)}; b_n^{(2)} \dots b_2^{(2)} b_1^{(2)}; \dots; b_n^{(k)} \dots b_2^{(k)} b_1^{(k)}\right] \tag{9}$$

The corresponding decimal population matrix is represented as follows:

$$\begin{bmatrix} \theta_1^{(1)} & \theta_2^{(1)} & \cdots & \theta_m^{(1)} \\ \theta_1^{(2)} & \theta_2^{(2)} & \ddots & \theta_m^{(2)} \\ \vdots & \vdots & \ddots & \vdots \\ \theta_1^{(k)} & \theta_2^{(k)} & \cdots & \theta_m^{(k)} \end{bmatrix} \tag{10}$$

(2) Individual Evaluation: All individuals in the population are fitted to the Kriging model using the sample points $\boldsymbol{x}$ and output responses $\boldsymbol{y}$ in their decimal form $\boldsymbol{\theta}^{(k)}$. The optimization function $\varphi(\boldsymbol{\theta})$ in the Kriging model is used as the fitness function to calculate the fitness value of each individual. The model and its corresponding individual fitness values are as follows:

$$\begin{cases} \hat{y}^{(1)}(\boldsymbol{x}) = f^{(1)^T}(\boldsymbol{x})\widehat{\boldsymbol{\beta}^{(1)}} + r^{(1)^T}(\boldsymbol{x})\boldsymbol{R}^{(1)^{-1}}\left(\boldsymbol{Y}-\boldsymbol{F}^{(1)}\widehat{\boldsymbol{\beta}^{(1)}}\right) \rightarrow \varphi_1\left(\boldsymbol{\theta}^{(1)}\right) \\ \hat{y}^{(2)}(\boldsymbol{x}) = f^{(2)^T}(\boldsymbol{x})\widehat{\boldsymbol{\beta}^{(2)}} + r^{(2)^T}(\boldsymbol{x})\boldsymbol{R}^{(2)^{-1}}\left(\boldsymbol{Y}-\boldsymbol{F}^{(2)}\widehat{\boldsymbol{\beta}^{(2)}}\right) \rightarrow \varphi_2\left(\boldsymbol{\theta}^{(2)}\right) \\ \vdots \\ \hat{y}^{(k)}(\boldsymbol{x}) = f^{(k)^T}(\boldsymbol{x})\widehat{\boldsymbol{\beta}^{(k)}} + r^{(k)^T}(\boldsymbol{x})\boldsymbol{R}^{(k)^{-1}}\left(\boldsymbol{Y}-\boldsymbol{F}^{(k)}\widehat{\boldsymbol{\beta}^{(k)}}\right) \rightarrow \varphi_k\left(\boldsymbol{\theta}^{(k)}\right) \end{cases} \tag{11}$$

(3) Selection: Select a portion of superior individuals to inherit to the next generation's new population, aiming to minimize the loss of superior genetic information. Roulette wheel selection is the most common method. The probability of different individuals being selected is calculated as follows:

$$P_k = \frac{\varphi_k\left(\boldsymbol{\theta}^{(k)}\right)}{\sum_{i=1}^{k}\varphi\left(\boldsymbol{\theta}^{(k)}\right)} \tag{12}$$

(4) Crossover: Perform crossover recombination on a portion of binary individual chromosomes to generate new individuals. The chromosomes of these new individuals are

inherited into the next generation to enhance population diversity. This paper applies single-point crossover with the formula representation as follows:

$$\text{Before Crossover:}\begin{cases}[b_n^{(u)} \dots b_g^{(u)} \dots b_2^{(u)} b_1^{(u)}]\\ [b_n^{(w)} \dots b_g^{(w)} \dots b_2^{(w)} b_1^{(w)}]\end{cases} \rightarrow \text{After Crossover:}\begin{cases}[b_n^{(u)} \dots b_g^{(w)} \dots b_2^{(u)} b_1^{(u)}]\\ [b_n^{(w)} \dots b_g^{(u)} \dots b_2^{(w)} b_1^{(w)}]\end{cases} \tag{13}$$

In this context, $w$ and $u$ represent the $w$-th and $u$-th individuals in the population, selected through random sampling. Similarly, the number of gene positions $g$ for the crossover operation is also determined by random sampling.

(5) Mutation: Modify the values of certain gene positions in the binary chromosomes of some individuals. The chromosomes of the new individuals are introduced into the new population to enhance population diversity. The mutation process is illustrated in Fig. 1.

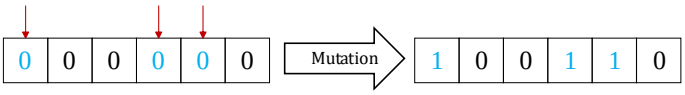


Fig. 1. Mutation diagram.

The individuals for mutation and the number of gene positions mutated are also determined by random sampling. Each individual can undergo multiple-point mutations, which are related to the set mutation probability.

(6) Iteration: Form a new population by selecting, crossing, and mutating individuals. Repeat the processes from (2) to (5) until the convergence criteria are met or the maximum number of iterations is reached, at which point the iteration terminates [15].

(7) Post-Processing: Re-evaluate the final population $\boldsymbol{\theta}^{(k)}$, sort the individuals based on their fitness values $\varphi_k$ ($\boldsymbol{\theta}^{(k)}$), and perform decoding. The individual with the maximum fitness value is the optimal Kriging correlation parameter $\boldsymbol{\theta}^*$, which is then used to establish the best Kriging model.

$$\widehat{y^*}(\boldsymbol{x}) = f^{*T}(\boldsymbol{x})\widehat{\boldsymbol{\beta}^*} + r^{*T}(\boldsymbol{x})\boldsymbol{R}^{*-1}\left(\boldsymbol{Y} - \boldsymbol{F}^*\widehat{\boldsymbol{\beta}^*}\right) \tag{14}$$

### 2.3. DCGAK

This paper introduces the Distributed Collaborative (DC) strategy into the GAK model to further improve the accuracy and computational efficiency of reliability analysis [16]. The DC strategy is mainly used to address complex problems that are high-dimensional and highly nonlinear. It decomposes a complex problem into several simpler and solvable sub-problems, clearly defining the input variables and output responses for each level of sub-problems. The distributed GAK model is trained and fitted step-by-step. The models at each level are not isolated; the output response of the upper-level model is used as the input for the next-level model. Ultimately, these sub-problems are collaboratively integrated to establish the DCGAK model.

DCGAK decomposes a complex probabilistic problem into $l$ levels of simpler probabilistic analysis problems [17], as shown in Fig. 2. Let $\boldsymbol{x}^{(l)}$ ($\boldsymbol{x}^{(l)} \in \mathbb{R}^n$) be the input variable vector for the $l$-th level structure, and $\boldsymbol{y}^{(l)}$ ($\boldsymbol{y}^{(l)} \in \mathbb{R}^p$) be the output response for the $l$-th level structure. The optimization of Kriging model correlation parameters $\boldsymbol{\theta}^{(k)}$ is performed using genetic algorithms. The $i$-th output response $y_i^{(1)}$($i$=1,2,…,$p_1$) at the first level can be expressed as:

$$y_i^{(1)} = \hat{y}\left(\boldsymbol{x}^{(1)}\right) = f\left(\boldsymbol{x}^{(1)}\right)^T \hat{\beta}_i^{(1)} + r\left(\boldsymbol{x}^{(1)}\right)^T (R_i^{(1)})^{-1} \left(Y_i^{(1)} - F_i^{(1)}\hat{\beta}_i^{(1)}\right) \tag{15}$$

This is referred to as the first-level distributed GAK model (GAK-I), with the $i$-th output response corresponding to the input variables at the first level. Similarly, all GAKs-I models can be established in the following vector form:

$$\boldsymbol{y}^{(1)} = \left(y_1^{(1)}, y_2^{(1)}, \dots y_{p_1}^{(1)}\right)^T \tag{16}$$

where $p_1$ represents the number of first-level response outputs.

Based on the distributed collaborative strategy and the correlation with specific failure modes, the output response $\boldsymbol{y}^{(1)}$ of the first-level GAK model is used as the input random variable for the output response $\boldsymbol{y}^{(2)}$ of the second-level GAK model. Thus, the second-level output response $\boldsymbol{y}^{(2)}$ can be expressed as:

$$y_j^{(2)} = \hat{y}\left(\boldsymbol{y}^{(1)}\right) = f\left(\boldsymbol{y}^{(1)}\right)^T \hat{\beta}_j^{(2)} + r\left(\boldsymbol{y}^{(1)}\right)^T (R_j^{(2)})^{-1} \left(Y_j^{(2)} - F_j^{(2)}\hat{\beta}_j^{(2)}\right) \tag{17}$$

Similarly, the GAK model can be fitted between the $l$-th level output response $\boldsymbol{y}^{(l)}$ and the ($l$-1)-th level output response $\boldsymbol{y}^{(l-1)}$. The $k$-th output response $y_k^{(l)}$ at the $l$-th level can be expressed by the following equation:

$$y_s^{(l)} = \hat{y}\left(\boldsymbol{y}^{(l-1)}\right) = f\left(\boldsymbol{y}^{(l-1)}\right)^T \hat{\beta}_s^{(l)} + r\left(\boldsymbol{y}^{(l-1)}\right)^T (R_s^{(l)})^{-1} \left(Y_s^{(l)} - F_s^{(l)} \hat{\beta}_s^{(l)}\right) \quad (18)$$

Finally, based on the limit state function of the problem, the output response $\boldsymbol{y}^{(l)}$ of the $l$-th level GAK model is used as the input random variable for the global output response $Z$, constructing the global DCGAK model:

$$Z = \hat{y}\left(\boldsymbol{y}^{(l)}\right) = f\left(\boldsymbol{y}^{(l-1)}\right)^T \hat{\beta}_Z^{(Z)} + r\left(\boldsymbol{y}^{(l)}\right)^T (R_Z^{(Z)})^{-1} \left(Y_Z^{(Z)} - F_Z^{(Z)} \hat{\beta}_Z^{(Z)}\right) \quad (19)$$

In summary, the DCGAK model, based on a mathematical surrogate model, integrates the features of the distributed collaborative strategy and genetic algorithms, offering new ideas for the reliability analysis and optimization design of complex mechanical structures.

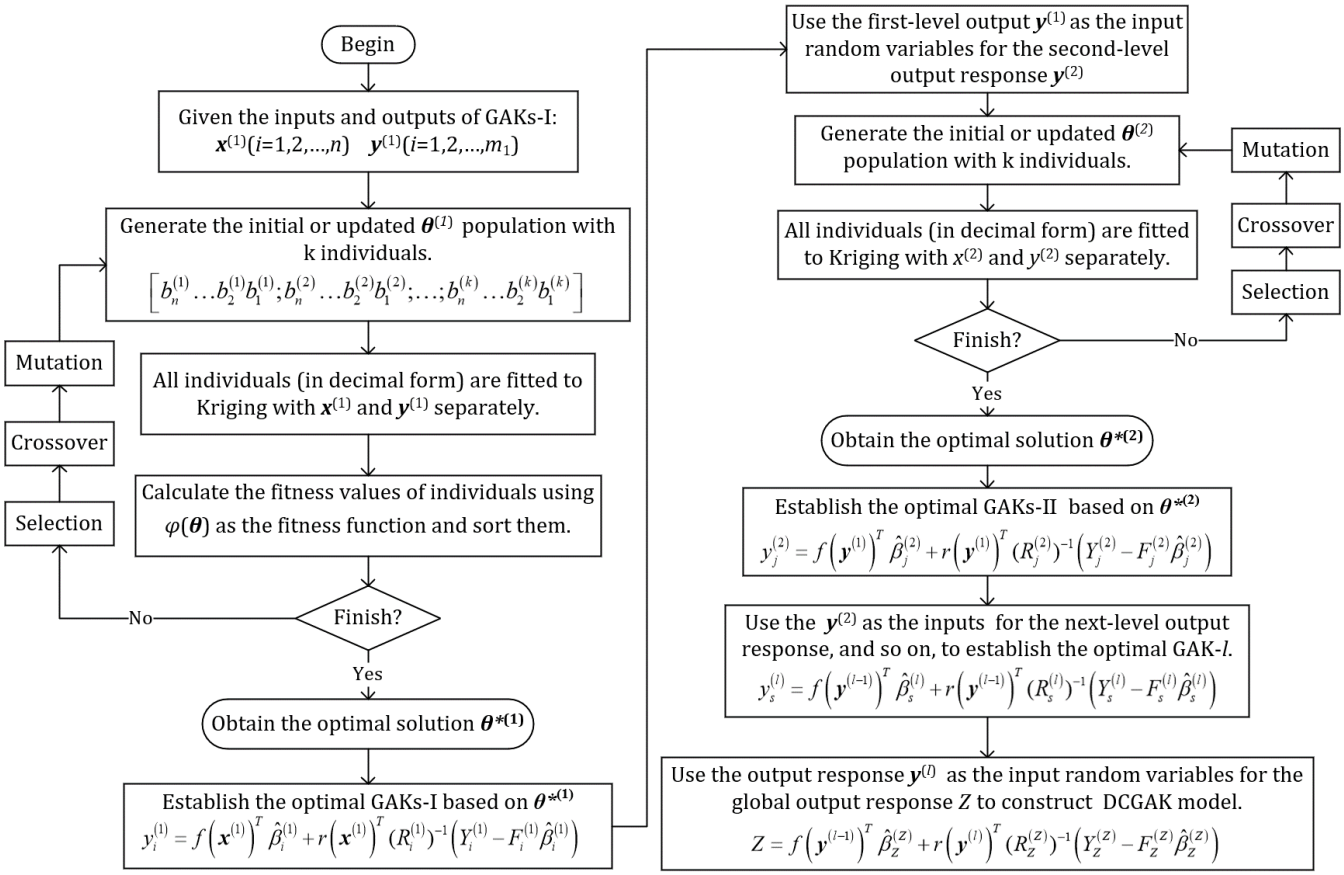


Fig. 2. DCGAK process flowchart.

### 2.4. Numerical example

To validate the effectiveness of the DCGAK model, an analysis was conducted on the cantilever tube structure strength problem described in the literature [33]. The model structure is shown in the Fig. 3. This problem is highly complex in terms of nonlinearity, with a large number of input variables and diverse distribution types, as shown in Table 1. For the Gaussian distribution, the parameters 1 and 2 refer to mean and standard deviation, respectively; For the uniform and interval distributions, the parameters 1 and 2 refer to the lower and upper bounds, respectively; For the Gumbel distribution, the parameters 1 and 2 refer to the location and size parameters, respectively.

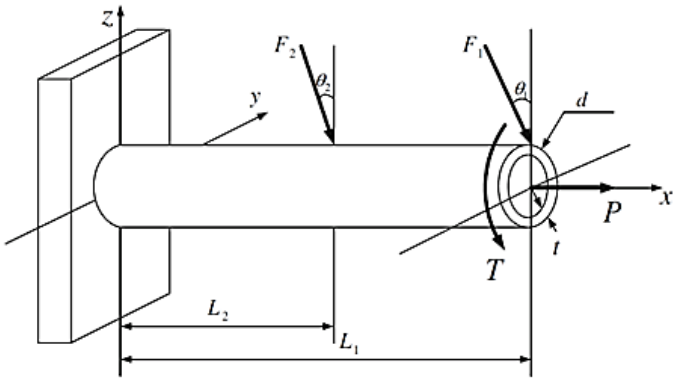


Fig. 3. Cantilever tube structure diagram.

Table 1. Random variables and distributions for the strength problem of the cantilever tube.

| Variable/Unit | Parameter 1 | Parameter 2 | Distribution |
|---|---|---|---|
| $t$/mm | 5 | 0.1 | Gaussian |
| $D$/mm | 42 | 0.5 | Gaussian |
| $\sigma_s$/MPa | 200 | 20 | Gaussian |
| $P$/N | 12000 | 1200 | Gaussian |
| $T$/N·m | 90 | 9 | Gaussian |
| $L_2$/mm | 59.75 | 60.25 | Uniform |
| $L_1$/mm | 119.75 | 120.25 | Interval |
| $\theta_1$/° | 0 | 10 | Interval |
| $\theta_2$/° | 5 | 15 | Interval |
| $F_1$/N | 3000 | 300 | Gumbel |
| $F_2$/N | 3000 | 300 | Gumbel |

The limit state function can be defined as:

$$G(\boldsymbol{X},\boldsymbol{Y}) = \sigma_s - \sigma_{mises} \tag{20}$$

In the equation, $\sigma_s$ represents the yield strength, and $\sigma_{mises}$ is the equivalent stress of the structure, which can be calculated as follows:

$$\sigma_{mises} = \sqrt{\sigma_x^2 + 3\tau_{zx}^2} \tag{21}$$

In the equation, $\tau_{zx}$ is the shear stress, and $\sigma_x$ is the normal stress, which can be calculated as follows:

$$\begin{cases} \tau_{zx} = \dfrac{TD}{4I} \\ \sigma_x = \dfrac{P + F_1\sin(\theta_1) + F_2\sin(\theta_2)}{A} + \dfrac{MD}{2I} \end{cases} \tag{22}$$

$$\begin{cases} M = F_1 L_1\cos(\theta_1) + F_2 L_2\cos(\theta_2) \\ A = \dfrac{\pi}{4}[D^2 - (D-2t)^2] \\ I = \dfrac{\pi}{64}[D^4 - (D-2t)^4)] \end{cases} \tag{23}$$

The DCGAK model was applied to the cantilever tube structure strength problem, using the input and output variables from equation (23) as the training targets for the first-level distributed GAK. In this level, parameters $M$, $A$, and $I$ can be parallelized to improve computational efficiency. The output response from the first level is then used as the input variable for the second-level output responses $\tau_{zx}$ and $\sigma_x$, allowing the training of the second-level distributed GAK. Finally, equation (21) is used as the collaborative GAK to establish the overall DCGAK prediction model. MCM sampling was used to generate 100 samples for model training and 50 samples for error validation. The MCM sample values served as the benchmark for accuracy. The table below compares the prediction errors of the global output response, $\sigma_{mises}$, for 50 samples across four different models: Kriging, DCKriging, GAK, and DCGAK.

Table 2. Table of error comparison in σmises prediction.

| Method | MCM | Kriging | DCKriging | GAK | DCGAK |
|---|---|---|---|---|---|
| RMSE | —— | 1.0291 | 0.6639 | 0.0752 | 0.1838 |
| MAPE | —— | 0.8662% | 0.6045% | 0.1635% | 0.0129% |

Substitute the 10,000 MCM basic variable samples into the trained DCGAK model to assess the reliability $R$ using the limit state function. The results are compared with MCM results as shown in Table 3.

Table 3. Table of relative precision in reliability prediction.

| Method | MCM | Kriging | DCKriging | GAK | DCGAK |
|---|---|---|---|---|---|
| Reliability $R$ | 0.9934 | 1.0000 | 0.9982 | 0.9882 | 0.9935 |
| Precision(%) | —— | 99.34 | 99.52 | 99.48 | 99.99 |

Tables 2. and 3. indicate that, in terms of both prediction error and reliability prediction accuracy, the DCGAK model outperforms the other three prediction models, with only minor differences from the MCM sample values. After employing the

distributed collaborative strategy, the prediction errors and reliability prediction accuracy of DCKriging and DCGAK surpass those of the corresponding Kriging and GAK models, respectively. These comparative results demonstrate the universality, feasibility, and effectiveness of DCGAK in enhancing computational accuracy.

## 3. Deterministic analysis of turbofan blades

### 3.1. Finite element model

In this paper, the turbofan blade of the CFM-56 turbofan engine is taken as the research object. The blade consists of the tip profile, inner profile, and root profile, with the blade root separated from the shank. A finite element (FE) model of the turbofan blade is established in the ANSYS simulation software, with the blade divided into hexahedral mesh elements of varying sizes. The mesh comprises 2784 nodes and 3596 elements, as shown in Fig. 4. The turbofan blade is made of aerospace titanium alloy, with mechanical properties such as Young's modulus $E$, density $\rho$, and Poisson's ratio $\mu$ being 112GPa, 4453 kg/m³, and 0.32, respectively.

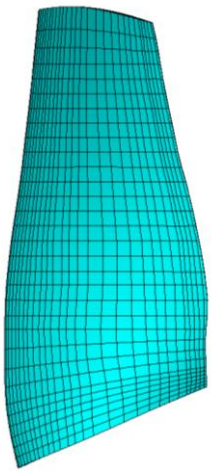

Fig. 4. Finite element model of the CFM-56 turbofan blades.

Material mechanical properties and load conditions exhibit randomness. The random variables affecting the vibration frequency of the turbofan blade primarily include: Young's modulus $E$, density $\rho$, Poisson's ratio $\mu$, and blade rotational speed $\omega$. Assuming that the random variables follow a Gaussian distribution, let the basic random vector be $\boldsymbol{x}=[E\ \rho\ \mu\ \omega]$. The statistical characteristics of these random variables are shown in Table 4.

Table 4. Statistical characteristics of random variables.

| Variable | Mean | Standard deviation | Distribution |
|---|---|---|---|
| Young's modulus $E$ | 112GPa | 2.24GPa | Gaussian |
| Density $\rho$ | 4453kg/m³ | 89.06kg/m³ | Gaussian |
| Poisson's ratio $\mu$ | 0.32 | 0.0064 | Gaussian |
| Rotational speed $\omega$ | 434.5870rad/s | 8.69174rad/s | Gaussian |

### 3.2. Modal and harmonic response analysis

To effectively perform modal analysis of the turbofan blade, the finite element model of the turbofan blade is fixed by constraining all degrees of freedom at the blade root. This allows for the analysis of the blade's natural frequencies under different centrifugal loads (i.e., different rotational speeds) and the construction of the Campbell diagram for the turbofan blade. In the Campbell diagram, the horizontal axis represents the rotational speed, and the vertical axis represents the frequency. The forced vibration component, which is related to the excitation frequency $f_w$ that depends on the rotational speed, is depicted as a blue ray emanating from the origin. The black curves represent the relationship between the natural frequencies of different modes and the rotational speed. As the mode number and rotational speed increase, the natural frequencies gradually increase, as shown in Fig. 5.

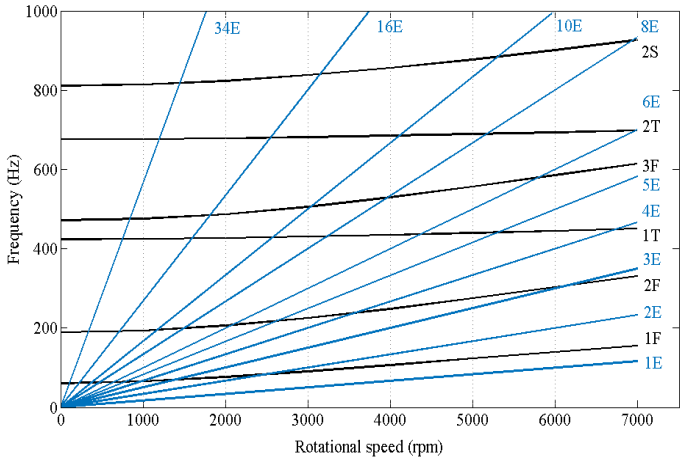


Fig. 5. Campbell diagram of the turbofan blade.

Extensive research by scholars both domestically and internationally has shown that resonance caused by the first three modes of the turbofan blade is a primary failure mode of the blade [18]. During normal engine operation, the turbofan blades typically run at a rotational speed of 4150 rpm (83% of the design speed). Harmonic response analysis of the turbofan blades is shown in Fig. 6., where resonance occurs at different levels for the first three modes, with corresponding frequencies of $f_1$=109.01Hz, $f_2$=252.14Hz and $f_3$=435.13Hz. Although the frequency response curve indicates that the vibration response is maximum during third-mode resonance, the amplitude of vibration without damping does not match actual conditions. Fig. 6. is used solely to determine the resonance frequencies. In operation, the turbofan blades are subjected to complex excitation loads, which can lead to resonance in the third mode alone or simultaneous resonance in the first, second, and third modes, resulting in greater vibration responses. Therefore, this paper considers both cases of third-mode resonance alone and simultaneous resonance in the first, second, and third modes for vibration stress analysis and performs fatigue strength reliability analysis for each case.

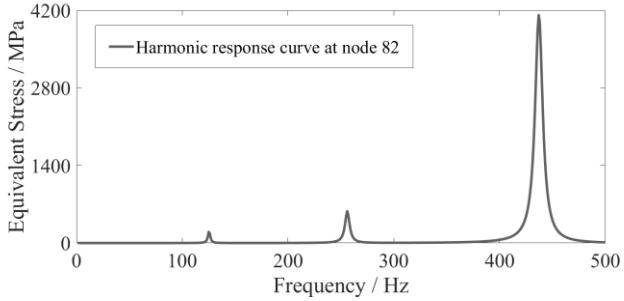


Fig. 6. Harmonic response curve at node 82.

### 3.3. Aerodynamic analysis

In general, total pressure disturbances are the most prevalent form of intake disturbances [19-21]. Current industrial tests emphasize steady-state disturbances, with circumferential disturbances exerting a more significant impact on structural stress responses compared to radial disturbances [22]. Moreover, circumferential total pressure disturbances primarily result in performance degradation of the aircraft engine [7]. Hence, this study focuses on steady-state circumferential total pressure intake disturbances, the disturbances $\vartheta$ is assumed to have a periodic cosine distribution in the circumferential direction, as shown in the following formula:

$$\vartheta = 1[\text{atm}] \times [1 + 0.1\cos(n' \cdot \theta_c)] \tag{24}$$

where $n'$ is the number of cosine disturbances experienced by the turbofan blade during one revolution.

According to the Campbell diagram, the second order excitation frequency of the blade is more likely to interfere with the first mode natural frequency at this speed; the fourth order excitation frequency is more likely to interfere with the second mode natural frequency; and the sixth order excitation frequency is more likely to interfere with the third mode natural frequency. The aerodynamic excitation frequency $f_w$ in the Campbell diagram can be expressed as the engine order $n$ multiplied by the rotor rotational frequency, i.e., $f_w=n\cdot\omega/2\pi$. Generally, the order $n$ of wake excitation is relatively high and corresponds to the number of blades. However, the excitation order $n$ caused by intake disturbances is generally low, making it easier to induce low-order mode resonance in the blades. When the excitation frequency $f_w$ is second order ($n$=2), the blades experience $n'$=2 disturbances per revolution [23], i.e., $n=n'$; similarly, for fourth and sixth order frequencies. The circumferential distribution disturbance curves under different disturbances and the corresponding aerodynamic load simulation results are shown in Fig. 7.

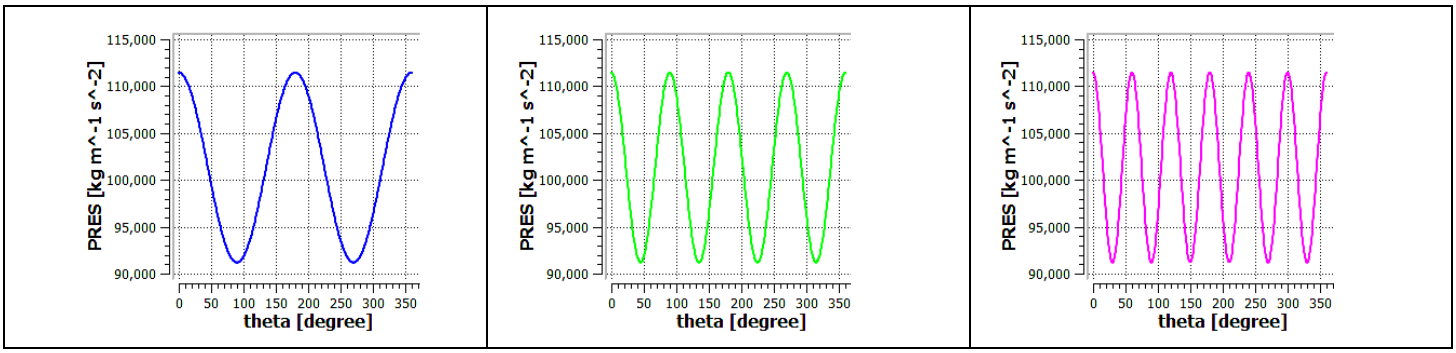

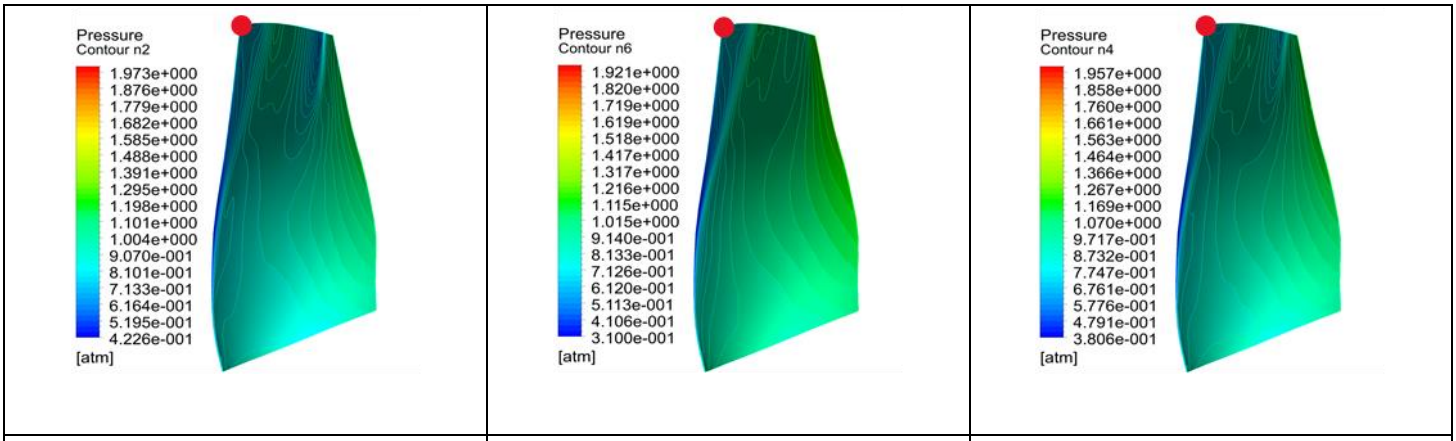


| $n$=$n'$=2 | $n$=$n'$=4 | $n$=$n'$=6 |
|---|---|---|

Fig. 7. Circumferential distribution disturbance curves and aerodynamic load distribution contour map.

As illustrated in Fig. 7., with an increase in the number of disturbances $n'$, both the maximum and minimum aerodynamic loads on the turbofan blade surface exhibit a certain degree of reduction. The variation in the aerodynamic load distribution on the suction surface primarily occurs near the blade tip. Despite the different numbers of disturbances experienced by the turbofan blades, the points of maximum aerodynamic load consistently appear at the red point near the blade tip in the figure.

### 3.4. Harmonic-transient coupling analysis

The harmonic response transient coupling analysis detailed in this paper is primarily employed to perform dynamic analysis on structures subjected to multiple sinusoidal loads of varying frequencies concurrently. Initially, the respective displacement solutions are obtained under the influence of each individual sinusoidal load. The displacement solutions are superimposed to acquire the total displacement solution. Subsequently, the corresponding stresses and strains at any given moment in the structure can be derived from the total displacement solution.

For the scenario where only third-order modal resonance occurs, the turbofan blade analysis requires the introduction of an aerodynamic load with a disturbance number $n$'=6. Conversely, when first, second, and third-order modal resonances occur simultaneously, aerodynamic loads with disturbance numbers $n$'=2,4 and 6 respectively, need to be incorporated for the harmonic response transient coupling analysis.

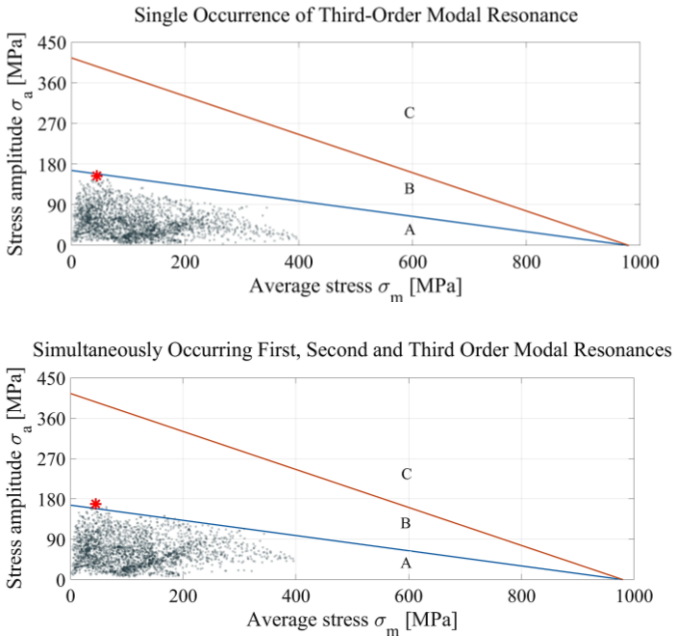


Fig. 8. Modified Goodman combined with stress scatter plots.

By utilizing the modified Goodman diagram for titanium alloys, the mean stress $\sigma_m$ and the actual vibratory stress amplitude $\sigma_{max}$ at each node of the blade are extracted and plotted as a scatter diagram, as illustrated in Fig. 8. Herein, $\sigma_{max}$ represents the maximum equivalent stress value in the time history of each node of the turbofan blade under different resonance modes, whereas $\sigma_m$ denotes the equivalent stress of the blade nodes considering only the centrifugal load.

In Fig. 8., regions A, B, and C respectively indicate areas where the vibratory stress amplitude is within the infinite life region, finite life region, and failure region. The red "*" denotes the most critical node of the blade. When the stress amplitude of the most critical node lies within region A, the blade is considered reliable. For the same mean stress $\sigma_m$, the value on

the blue line represents the alternating load limit $\sigma_{lim}$ corresponding to the most critical node, which can be expressed as:

$$\sigma_{lim} = -0.1693 \cdot \sigma_m + 166 \tag{25}$$

The mean stress $\sigma_m$, vibratory stress amplitude $\sigma_{max}$, and alternating load limit $\sigma_{lim}$ corresponding to the most critical node under two different resonance modes are shown in Table 5. In the table, $\sigma_{max}^{(3)}$ represents the stress amplitude when only third-order modal resonance occurs, while $\sigma_{max}^{(123)}$ represents the stress amplitude when first, second, and third-order modal resonances occur simultaneously.

Table 5. Stress data for the most critical node under two different resonance modes.

| $\sigma_{max}$ | Node | $\sigma_m$ / MPa | $\sigma_{max}$ / MPa | $\sigma_{lim}$ / MPa |
|---|---|---|---|---|
| $\sigma_{max}^{(3)}$ | Node82 | 44.4741 | 154.1441 | 158.4705 |
| $\sigma_{max}^{(123)}$ | Node82 | 44.4741 | 169.0441 | 158.4705 |

Fig. 8. indicates that the closer the node is to the "lower left," the safer it is, and the closer it is to the "upper right," the more dangerous it becomes. Additionally, the more and the more complex the resonance mode orders, the greater the number of nodes that may fail. Comparing the cases of only third-order modal resonance with the simultaneous occurrence of first, second, and third-order modal resonances, the latter scenario shows an overall upward shift in node positions, although the change is not significant. This suggests that the vibratory stress amplitude is primarily influenced by third-order modal resonance, which is corroborated by the harmonic response analysis results.

## 4. DCGAK-based fatigue strength reliability assessment

### 4.1. Reliability assessment framework

This paper optimizes the Kriging model parameters using a genetic algorithm and combines it with the DC strategy to account for the uncertainties of variables related to the turbofan blade, thereby studying the fatigue strength reliability assessment of the turbofan blade considering intake disturbances. The framework is shown in Fig. 9.

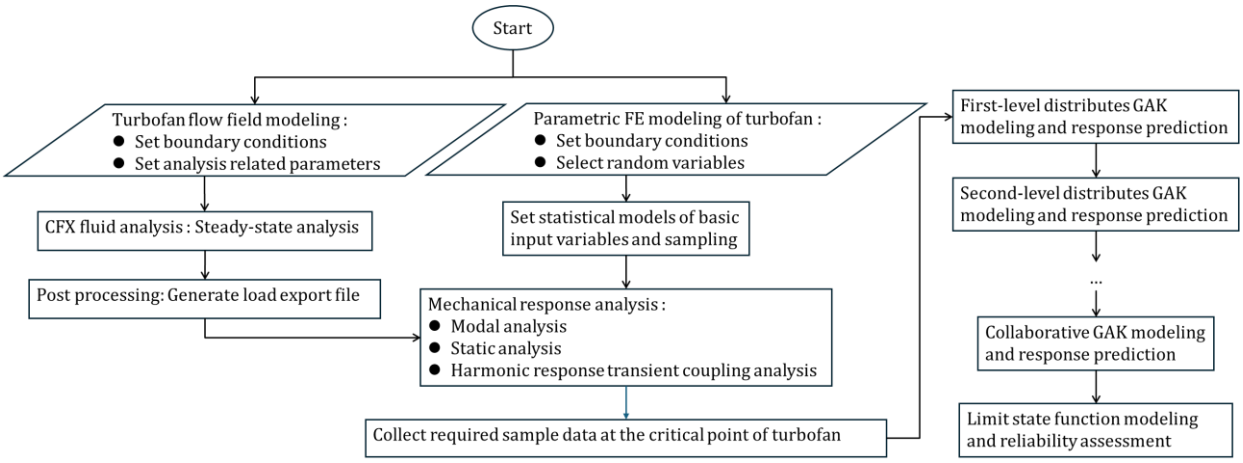


Fig. 9. Reliability assessment framework plot.

Firstly, the modal analysis results of the turbofan blade, specifically the natural frequencies $f_i$ of the first three modes, and the mean stress $\sigma_m$ at the most critical node of the turbofan blade are taken as the first-level output responses, which can be parallelly calculated to improve computational efficiency. The elastic modulus $E$, density $\rho$, Poisson's ratio $\mu$, and blade rotational speed $\omega$ are considered as the first-level input variables. Consequently, the first-level Genetic Algorithm-based Kriging (GAK) model is established:

$$f_i = f_i(E, \rho, \mu, \omega) \qquad i = 1,2 \; or \; 3 \tag{26}$$

$$\sigma_m = \sigma_m(E \; \rho \; \mu \; \omega) \tag{27}$$

Based on the DCGAK model principle, the first-level output responses are used as the input variables for the second-level GAK model. The second-level output responses are the vibratory stress amplitude $\sigma_{max}$ at the most critical node under two different resonance modes obtained through finite element analysis, and the alternating load limit $\sigma_{lim}$ calculated using equation (25), which can be computed in parallel, to establish the second-level GAK model:

$$\sigma_{max} = \begin{cases} \sigma_{max}(E, \rho, \mu, f_3) \\ \sigma_{max}(E, \rho, \mu, f_1, f_2, f_3) \end{cases} \tag{28}$$

$$\sigma_{lim} = \sigma_{lim}(\sigma_m) \tag{29}$$

Based on the limit state function of the strength interference theory, the global response DCGAK model is established:

$$Z = \sigma_{lim} - \sigma_{max} \tag{30}$$

The 100 sets of samples obtained from LHS sampling are used for training to establish the DCGAK model for fatigue strength failure reliability analysis. Subsequently, 10,000 sets of sampled data are input into the model, and the fatigue strength reliability is ultimately calculated using the following formula:

$$R = 1 - P_f = 1 - \frac{1}{M}\sum_{k=1}^{M} I_F[Z_k] = 1 - \frac{m}{M} \tag{31}$$

where $I_F[Z_k]$ is the indicator function that can be expressed as:

$$I_F[Z_k] = \begin{cases} 1, & Z < 0 \\ 0, & Z \geq 0 \end{cases} \tag{32}$$

### 4.2. Distributed GAK modeling

The first-level output responses are the natural frequencies $f_i$ of the first three modes of the turbofan blade. Using LHS, 100 sets of input-output samples are sampled for training the first-level distributed GAK, and 50 sets are used to verify the GAK fitting accuracy. The fitting relationship between the predicted output and the target output is shown in the Fig. 10.

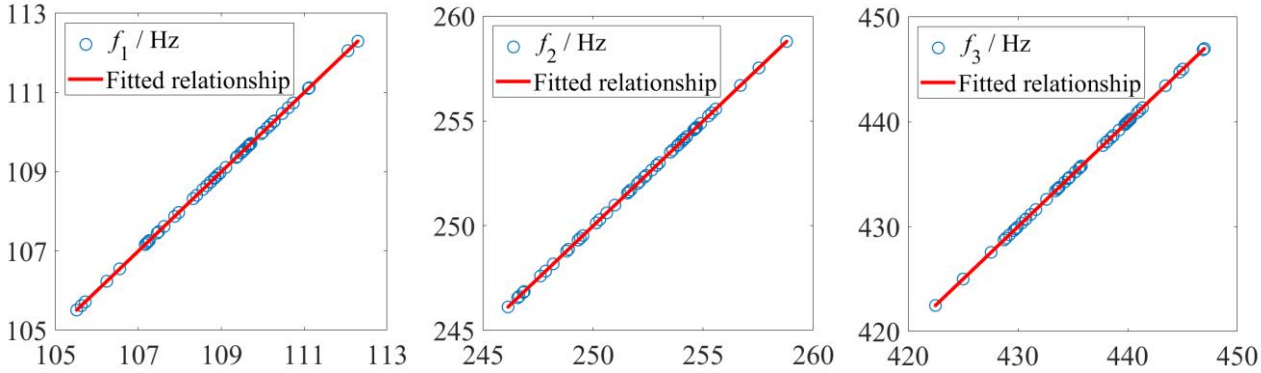


Fig. 10. Comparison of predicted output and target output about the first three modes.

Table 6. Comparison of model characteristics for different algorithms.

| Algorithms | Correlation coefficient matrix $\boldsymbol{\theta}$ | Regression coefficient matrix $\boldsymbol{\beta}$ | Process variance matrix $\boldsymbol{\sigma^2}$ |
|---|---|---|---|
| Kriging | [0.059,0.0058,0.001,0.0013] | [0.3999,1.4471,2.0564] | [86.3431,209.3466,7.3411] |
| GAK | [0.001,0.001,0.001,0.001] | [0.5830,2.2264,3.1934] | [103.6428,248.5088,9.5089] |

It can be observed that the optimized Kriging model provides a high level of accuracy in predicting outputs compared to target outputs and is suitable for regression predictions. Using the MCM sampling results as the reference solution, the prediction errors for 50 sample sets from different algorithms are compared. The model characteristics are shown in Table 6.

Validation shows that the root mean square error (RMSE) and mean percentage error (MAPE) for 50 validation samples using Kriging are 3.8389e-03 and 1.6775e-04%, respectively. For the same validation samples, the corresponding results for GAK are 6.4783e-05 and 3.4604e-06%. It can be seen that the GAK model exhibits better error accuracy compared to the Kriging prediction model, with performance comparable to MCM. This indicates the GAK model has strong learning and generalization capabilities and can be widely applied to function regression, numerical prediction, and reliability analysis.

### 4.3. Distributed response prediction

Based on the DCGAK reliability assessment framework, the Kriging surrogate models are trained in stages. The 10,000 sets of input variable samples are input into the DCGAK model to predict the output responses at each level. The natural frequencies of the first three modes of the turbofan blade, along with their probability distributions and statistical characteristics, are shown in Fig. 11. and Table 7. In Fig. 11., the red curve represents the fitted probability density curve, and the green curve represents the cumulative distribution curve. Within the allowable error range, the natural frequencies $f_i$ of the first three modes can be approximated as following a Gaussian distribution.

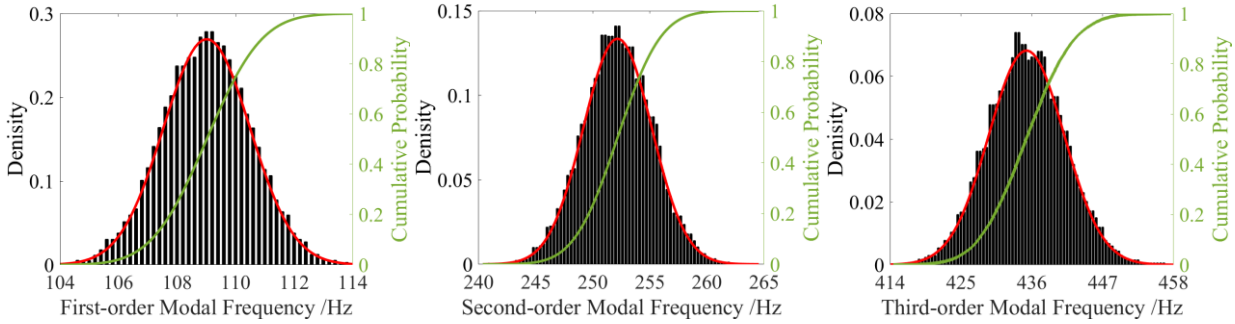


Fig. 11. Histogram of the probability distribution of the natural frequencies for the first three modes.

Table 7. Statistical characteristics of the natural frequencies for the first three modes.

| $f_i$ | Mean(Hz) | Std.(Hz) | Maximum(Hz) | Minimum(Hz) | Distribution |
|---|---|---|---|---|---|
| $f_1$ | 109.0143 | 1.4808 | 114.2777 | 103.5458 | Gaussian |
| $f_2$ | 252.1677 | 2.9882 | 264.2525 | 240.7481 | Gaussian |
| $f_3$ | 435.1759 | 5.8476 | 457.6117 | 414.4949 | Gaussian |

Table 8. Statistical characteristics of two types of stress.

| $\sigma_{max}$ | Mean(MPa) | Std. (MPa) | Maximum(MPa) | Minimum(MPa) | Distribution |
|---|---|---|---|---|---|
| $\sigma_{max}^{(3)}$ | 153.7005 | 6.2314 | 178.6057 | 125.3400 | Burr |
| $\sigma_{max}^{(123)}$ | 168.3171 | 6.2112 | 194.6983 | 145.9276 | Gaussian |

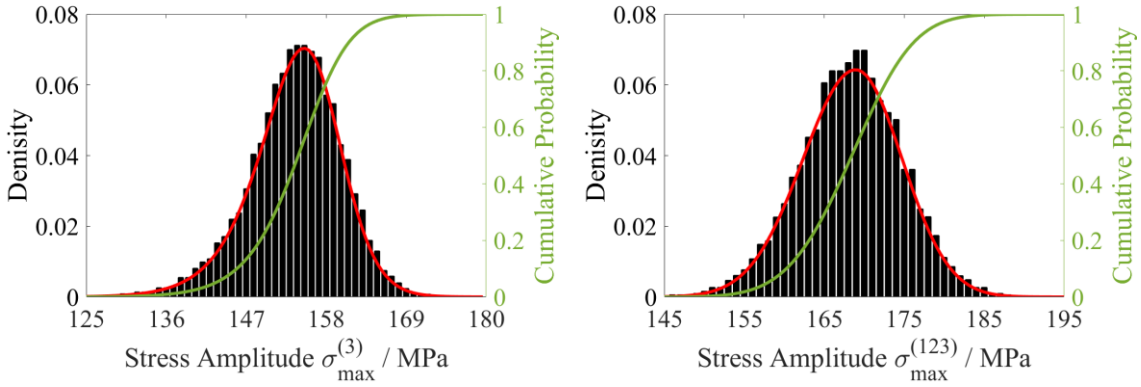


Fig. 12. Probability distributions of the two types of $\sigma_{max}$.

The probability distribution of the vibratory stress amplitude $\sigma_{max}$ at the most critical node under two different resonance modes is shown in Fig. 12. The red curve represents the fitted probability density curve, while the green curve represents the cumulative distribution curve. Within a certain error range, $\sigma_{max}^{(3)}$ can be approximated by a Burr distribution with scale parameter 159.052, first shape parameter 35.5769, and second shape parameter 2.43579. $\sigma_{max}^{(123)}$ can be approximated by a normal distribution, with its statistical characteristics detailed in Table 8.

By calculating the fatigue strength reliability for two different stress amplitudes using formulas (30)-(32), the fatigue strength reliability $R^{(3)}$ for third-order modal resonance alone is found to be 0.7935, while the fatigue strength reliability $R^{(123)}$ for simultaneous first, second, and third-order modal resonances is 0.0545. Thus, as the number and complexity of resonance modes increase, the vibratory stress amplitude $\sigma_{max}$ at the most critical node becomes larger, making the node more susceptible to fatigue strength failure. When first, second, and third-order modal resonances occur simultaneously, the excessive vibratory stress amplitude at the most critical node can lead to significant fatigue failure. To mitigate this, designers can reduce the vibratory response by avoiding resonance points, improving structural design, altering material properties, or implementing heat treatments.

### 4.4. Reliability assessment and comparison

The MCM method generates random input variables based on known probability distributions through repeated finite element simulations to obtain sample solutions, providing accurate and reliable results. To verify the effectiveness and feasibility of the proposed method, 10,000 MCM sample values are used as

a reference solution to compare the prediction precision of fatigue strength reliability R for Kriging, DCKriging, GAK, and DCGAK models. The input variables for Kriging and GAK models include elastic modulus $E$, density $\rho$, Poisson's ratio $\mu$, and blade rotational speed $\omega$. The comparison is shown in Table 9.

Table 9. Comparison of prediction precision for fatigue strength reliability R.

| Method | MCM | Kriging | | DCKriging | | GAK | | DCGAK | |
|---|---|---|---|---|---|---|---|---|---|
| $R$ | Value | Value | Precision | Value | Precision | Value | Precision | Value | Precision |
| $R^{(3)}$ | 0.7935 | 0.7931 | 99.96% | 0.7932 | 99.97% | 0.7935 | 100% | 0.7935 | 100% |
| $R^{(123)}$ | 0.0545 | 0.0535 | 98.21% | 0.0540 | 99.11% | 0.0545 | 100% | 0.0545 | 100% |

The prediction accuracy of both GAK and DCGAK models reaches 100%. Additionally, after employing the distributed collaborative strategy, the prediction accuracy of DCKriging is slightly superior to that of Kriging. This analysis demonstrates the feasibility of the distributed collaborative strategy for handling nonlinear and high-dimensional problems.

## 5. Conclusion

This paper develops an accurate and effective numerical prediction and reliability probability analysis method. Based on the Kriging surrogate model, the method employs a genetic algorithm (GA) to optimize the parameters of the Kriging model. These parameters directly influence the prediction accuracy of the Kriging model. Building on this, the Kriging model is combined with a distributed collaborative strategy to establish the DCGAK model.

A deterministic analysis of the turbofan blade revealed that as the mode order and rotational speed increase, the natural frequencies of the turbofan blade gradually increase. At a rotational speed of 4150 rpm, the first three modes of the turbofan blade experience varying degrees of resonance, with corresponding frequencies of $f_1$=109.01Hz, $f_2$=252.14Hz and $f_3$=435.13Hz. For aerodynamic analysis, although the turbofan blade experiences different numbers of disturbances, the maximum aerodynamic load always occurs at the blade tip.

Probabilistic analysis of the turbofan blade's first three natural frequencies and the vibratory stress amplitudes under two vibration modes shows that, within an allowable error range, the first three mode natural frequencies can be approximated by a normal distribution. Additionally, within a certain error range, $\sigma_{max}^{(3)}$ can be approximated by a Burr distribution with scale parameter 159.052, first shape parameter 35.5769, and second shape parameter 2.43579; whereas $\sigma_{max}^{(123)}$ approximates a normal distribution.

The DCGAK method addresses high-dimensional and nonlinear complex problems by breaking them down into simpler subproblems, thereby improving the computational efficiency and accuracy of reliability analysis for complex mechanical systems. For the turbofan blade case study presented in this paper, the reliability assessment accuracy of DCGAK reaches 100%. DCGAK can provide predicted sample values for intermediate steps according to the case analysis process, and parallel computing among distributed levels can enhance computational efficiency. These results demonstrate the universality and effectiveness of DCGAK, enriching the reliability analysis methods for complex mechanical systems.

In future research, more efficient and better-performing optimization algorithms can be employed based on the findings of this study. Additionally, custom nonlinear basis functions can be used to construct Kriging surrogate models with improved predictive capabilities. When conducting reliability analysis, the degradation of blades during long-term use was not considered in this paper. In the future, random modeling and analysis of the blade degradation process can be studied, such as accelerated degradation testing [34-36]. The current study focuses on either verifying the fatigue strength of the blade's vibration response or avoiding the natural frequency to prevent resonance, considering each aspect in isolation. Future studies can integrate these two failure analyses based on the relationship between the two failure mechanisms.

**Acknowledgements**

This paper is co-supported by the National Natural Science Foundation of China (Grant no. 51705309), and the China Postdoctoral Science Foundation (Grant no. 2017M621481). The authors would like to thank them.

## References


1. Gao H, Bai G. Reliability analysis on resonance for low-pressure compressor rotor blade based on least squares support vector machine with leave-one-out cross-validation. Advances in Mechanical Engineering 2015; 7(4): 1687814015578351, https://doi.org/10.1177/1687814015578351.
2. Gao H, Bai G. Vibration reliability analysis for aeroengine compressor blade based on support vector machine response surface method. Journal of Central South University 2015; 22(5): 1685-1694, https://doi.org/10.1007/s11771-015-2687-3.
3. Gao H F, Wang A, Zio E, et al. Fatigue strength reliability assessment of turbo-fan blades by Kriging-based distributed collaborative response surface method. Eksploatacja i Niezawodnosc – Maintenance and Reliability 2019; 21(3): 530-538, https://doi.org/10.17531/ein.2019.3.20.
4. Xu D, He C, Sun D, et al. Stall inception prediction of axial compressors with radial inlet distortions. Aerospace Science and Technology 2021; 109: 106433, https://doi.org/10.1016/j.ast.2020.106433.
5. Gu B, Xu D, Dong X, et al. A modified small perturbation stability prediction model for axial compressors with circumferential inlet distortion. Aerospace Science and Technology 2023; 132: 108079, https://doi.org/10.1016/j.ast.2022.108079.
6. Su G, Sun D, Li Y, et al. Aeroelastic stability of labyrinth seal ring under steady and dynamic total pressure intake distortion conditions. Mechanical Systems and Signal Processing 2023; 204: 110776, https://doi.org/10.1016/j.ymssp.2023.110776.
7. Doll U, Migliorini M, Baikie J, et al. Non-intrusive flow diagnostics for unsteady inlet flow distortion measurements in novel aircraft architectures. Progress in Aerospace Sciences 2022; 130: 100810, https://doi.org/10.1016/j.paerosci.2022.100810.
8. Ren L H, Ye Z F, Zhao Y P. A modeling method for aero-engine by combining stochastic gradient descent with support vector regression. Aerospace Science and Technology 2020; 99: 105775, https://doi.org/10.1016/j.ast.2020.105775.
9. Lu C, Teng D, Keshtegar B, et al. Extremum hybrid intelligent-inspired models for accurate predicting mechanical performances of turbine blisk. Mechanical Systems and Signal Processing 2023; 190: 110136, https://doi.org/10.1016/j.ymssp.2023.110136.
10. Lu C, Fei C W, Liu H T, et al. Moving extremum surrogate modeling strategy for dynamic reliability estimation of turbine blisk with multi-physics fields. Aerospace Science and Technology 2020; 106: 106112, https://doi.org/10.1016/j.ast.2020.106112.
11. Teng D, Feng Y W, Lu C, et al. Generative adversarial surrogate modeling framework for aerospace engineering structural system reliability design. Aerospace Science and Technology 2024; 144: 108781, https://doi.org/10.1016/j.ast.2023.108781.
12. Billinton R, Wang P. Teaching distribution system reliability evaluation using Monte Carlo simulation. IEEE Transactions on Power Systems 1999; 14(2): 397-403, https://doi.org/10.1109/59.761856.
13. Chen Z, He J, Li G, et al. Fast convergence strategy for adaptive structural reliability analysis based on kriging believer criterion and importance sampling. Reliability Engineering & System Safety 2024; 242: 109730, https://doi.org/10.1016/j.ress.2023.109730.
14. Michael S L. Statistical interpolation of spatial data: some theory for Kriging. 1999.
15. Cui D, Wang G, Lu Y, et al. Reliability design and optimization of the planetary gear by a GA based on the DEM and Kriging model. Reliability Engineering & System Safety 2020; 203: 107074, https://doi.org/10.1016/j.ress.2020.107074.
16. Song L K, Bai G C, Fei C W. Multi-failure probabilistic design for turbine bladed disks using neural network regression with distributed collaborative strategy. Aerospace Science and Technology 2019; 92: 464-477, https://doi.org/10.1016/j.ast.2019.06.026.
17. Gao H F, Wang Y H, Li Y, et al. Distributed-collaborative surrogate modeling approach for creep-fatigue reliability assessment of turbine blades considering multi-source uncertainty. Reliability Engineering & System Safety 2024; 250: 110316, https://doi.org/10.1016/j.ress.2024.110316.
18. Huang H M, Jiao W. Experiment and FEM analysis for fracture of fan blades. Advanced Materials Research, 2011; 143: 819-823, https://doi.org/10.4028/www.scientific.net/AMR.143-144.819.
19. Longley J P, Shin H W, Plumley R E, et al. Effects of rotating inlet distortion on multistage compressor stability. Journal of Turbomachinery 1996; 118: 181–188, https://doi.org/10.1115/1.2836624.
20. Dong X, Sun D, Li F, et al. Stall margin enhancement of a novel casing treatment subjected to circumferential pressure distortion. Aerospace Science and Technology 2018; 73: 239-255, https://doi.org/10.1016/j.ast.2017.12.005.
21. Peters T, Bürgener T, Fottner L. Effects of rotating inlet distortion on a 5-Stage HP-Compressor, American Society of Mechanical Engineers Digital Collection 2014, https://doi.org/10.1115/2001-GT-0300.

22. Reid C. The response of axial flow compressors to intake flow distortion. American society of Mechanical Engineers 1969, https://doi.org/10.1115/69-GT-29.
23. Fang M, Wang Y. Efficient numerical prediction of blade forced response under inlet distortion. Aerospace Science and Technology 2023; 142: 108612, https://doi.org/10.1016/j.ast.2023.108612.
24. Li X, Li W, Imran Lashari M, et al. Fatigue failure behavior and strength prediction of nickel-based superalloy for turbine blade at elevated temperature. Engineering Failure Analysis 2022; 136: 106191, https://doi.org/10.1016/j.engfailanal.2022.106191.
25. Wang Y, Song L, Li X, Bai G. Probabilistic fatigue estimation framework for aeroengine bladed discs with multiple fuzziness modeling. Journal of Materials Research and Technology 2023; 24: 2812–2827, https://doi.org/10.1016/j.jmrt.2023.03.196.
26. Zhu S, Liu Q, Peng W, Zhang X. Computational-experimental approaches for fatigue reliability assessment of turbine bladed disks. International Journal of Mechanical Sciences 2018; 142: 502-517, https://doi.org/10.1016/j.ijmecsci.2018.04.050.
27. Guo J, Zan X, Wang L, et al. A random forest regression with bayesian optimization-based method for fatigue strength prediction of ferrous alloys. Engineering Fracture Mechanics 2023; 293: 109714, https://doi.org/10.1016/j.engfracmech.2023.109714.
28. Ma Y, Zhang D, Hong J, Chen L. Prediction on high cycle life of blades using probability method. Journal of Propulsion Technology 2009; 30(4): 462-467, https://doi.org/10.13675/j.cnki.tjjs.2009.04.012.
29. Liu Y, Lao D, Yang C, et al. Harmonic resonance and high cycle fatigue of a radial turbine in pressure fluctuation. Transactions of Beijing Institute of Technology 2014; 34(11): 1120-1124, https://doi.org/10.15918/j.tbit1001-0645.2014.11.005.
30. Phan, H. M., and He, L. Investigation of structurally and aerodynamically mistuned oscillating cascade using fully coupled method. Journal of Engineering for Gas Turbines and Power 2022; 144(3): 031009, https://doi.org/10.1115/1.4052751.
31. Lin, J. Fatigue life assessment and reliability analysis of fan blades in turbofan engines. Tianjin University 2013.
32. Zhang M, Hou A, He X, et al. Intensity analysis of blades in axial compressor with inlet distortion. Journal of Aerospace Power 2011; 26(1): 108-114, https://doi.org/10.13224/j.cnki.jasp.2011.01.015.
33. Du, X. Unified uncertainty analysis by the first order reliability method. Journal of Mechanical Design 2008; 130(9): 091401, https://doi.org/10.1115/1.2943295.
34. Li Y, Xu S, Chen H, et al. A general degradation process of useful life analysis under unreliable signals for accelerated degradation testing. IEEE Transactions on Industrial Informatics 2023; 19(6): 7742-7750, https://doi.org/10.1109/TII.2022.3224960.
35. Li Y, Gao H, Chen H, et al. Accelerated degradation testing for lifetime analysis considering random effects and the influence of stress and measurement errors. Reliability Engineering & System Safety 2024; 247: 110101, https://doi.org/10.1016/j.ress.2024.110101.
36. Li Y, Fei M, Jia L, et al. Novel outlier-robust accelerated degradation testing model and lifetime analysis method considering time-stress-dependent factors. IEEE Transactions on Industrial Informatics 2024; 20(8): 9907-9917, https://doi.org/10.1109/TII.2024.3384611.

**Nomenclature**

| | | | |
|---|---|---|---|
| GA | Genetic Algorithm | $f_1$ | First-order natural frequency |
| GAK | GA-based Kriging model | $f_2$ | Second-order natural frequency |
| DCGAK | Distributed collaborative GAK | $f_3$ | Third order natural frequency |
| SVM | Support vector machine | $\vartheta$ | Intake disturbance pressure value |
| RFR | Random forest regression | $f_w$ | Excitation frequency |
| MCS | Monte Carlo simulation | $\sigma_m$ | Mean stress |
| $E$ | Young's modulus | $\sigma_{lim}$ | Alternating load limit |
| $\rho$ | Density | $\sigma_{max}$ | Vibratory stress amplitude |
| $u$ | Poisson's ratio | RMSE | Root mean square error |
| $\omega$ | Rotational speed | MAPE | Mean absolute percentage error |